

Tuning of strong nonlinearity in radio-frequency superconducting-quantum-interference-device meta-atoms

Ethan Zack,^{1,*} Daimeng Zhang,¹ Melissa Trepanier,¹ Jingnan Cai,¹ Tamin Tai,¹ Nikos Lazarides,² Johanne Hizanidis,² and Steven M. Anlage^{1,†}

¹*Quantum Materials Center, Department of Physics, University of Maryland, College Park, Maryland 20742-4111, USA*

²*Department of Physics, University of Crete, 71003 Herakleio, Greece*



(Received 17 December 2021; accepted 11 March 2022; published 6 April 2022)

Strong nonlinearity of a self-resonant radio-frequency (rf) superconducting-quantum-interference-device (SQUID) meta-atom is explored via intermodulation (IM) measurements. Previous work in zero dc magnetic flux showed a sharp onset of IM response as the frequency sweeps through the resonance. A second onset at higher frequency was also observed, creating a prominent gap in the IM response. By extending those measurements to nonzero dc flux, different dynamics are revealed, including dc flux tunability of the aforementioned gaps and enhanced IM response near geometric resonance of the rf SQUID. These features observed experimentally are understood and analyzed theoretically through a combination of a steady-state analytical modeling and a full numerical treatment of the rf SQUID dynamics. The latter in addition predicts the presence of chaos in narrow parameter regimes. The understanding of intermodulation in rf SQUID metamaterials is important for producing low-noise amplification of microwave signals and tunable filters.

DOI: [10.1103/PhysRevE.105.044202](https://doi.org/10.1103/PhysRevE.105.044202)

I. INTRODUCTION

Metamaterials were originally developed as a means to create novel interactions between matter and electromagnetic (EM) radiation [1–4]. It became clear that these novel interactions are particularly stark and dramatic in the case of metamaterials composed of superconducting meta-atoms [5]. Superconductors offer low loss and the ability to create compact meta-atoms due to their high critical current densities [6], thus ensuring that the metamaterial limit constraint (meta-atom size much less than EM wavelength) is satisfied [7,8]. In addition, superconductors bring both macroscopic and microscopic *quantum* effects into the largely classical field of metamaterial research [9]. The macroscopic quantum effects include magnetic flux quantization and the Josephson effects. These two macroscopic properties are elegantly combined in a single meta-atom known as a radio-frequency (rf) superconducting quantum interference device (SQUID). Radio-frequency SQUIDs are free-standing superconducting loops interrupted by a single Josephson junction [10]. As such, they are essentially split-ring resonators in which the capacitor is replaced with a Josephson junction to create a unique meta-atom. The junction essentially acts as a parallel combination of a fixed capacitance, a fixed resistance, and an ideal nonlinear inductor that can be tuned to explore both positive and negative values of inductance, including $\pm\infty$. The combination of geometrical and Josephson inductance, along with geometrical and Josephson capacitance, creates a self-resonant object that can oscillate with low loss in the

microwave regime. This simple device enables a nonlinear and tunable meta-atom, thus establishing an entirely new class of metamaterials [11,12]. As an added benefit, rf SQUID metamaterials can have strong and long-range interactions between the meta-atoms, which creates collective responses that can dramatically alter their interactions with EM fields. These interactions are also strongly nonlinear, making rf SQUID metamaterials a unique platform for the study of nonlinear physics involving many degrees of freedom. A number of review articles have appeared on superconducting metamaterials and the realization of quantum effects in these unique engineered materials [6,9,13].

The individual rf SQUID meta-atoms, as well as metamaterials made from these meta-atoms, have demonstrated a number of remarkable properties. The individual rf SQUIDs demonstrate extraordinarily broad tuning of their resonant frequency with both dc and rf magnetic flux [14–16]. The dc flux tunability is periodic, repeating every time the rf SQUID is punctuated by an integer number of flux quanta $\Phi_0 = h/2e$, where h is Planck's constant and e is the electronic charge. This tunability, accompanied by the intrinsic nonlinearity of the Josephson effect, leads to bistability [17,18] and multistability [19,20] in its response to rf and dc driving fields. This in turn leads to complex and hysteretic behavior, including the phenomenon of transparency [21]. Theory predicts that, under appropriate circumstances, driven rf SQUIDs will display strange nonchaotic attractors [22] and chaos [23,24].

Gathering the rf SQUIDs into a metamaterial can create a number of interesting properties. These center around the question of whether a large array of interacting nominally identical rf SQUIDs will oscillate coherently or incoherently when driven by a uniform global rf and dc flux. For example, a finite-size array will show strong edge effects because

*ezack@terpmail.umd.edu

†anlage@umd.edu

SQUIDs in the center and edges of the metamaterial will experience very different local magnetic environments [25]. Despite the disorder created by edges and defective SQUIDs, one can still observe coherent oscillations under strong rf drive [26]. Alternatively, complex spatial patterns created by disorder and inhomogeneous excitation with rf fields have been predicted [17,27,28] and visualized by laser scanning microscopy [29,30]. One of the most surprising spatiotemporal patterns concerns chimera states of the metamaterial. In this case a metamaterial made up of identical meta-atoms under uniform excitation will spontaneously break into domains of coherent oscillation intermingled with incoherent behavior [31–37].

Radio-frequency SQUIDs and rf SQUID metamaterials have been considered for applications as well. Examples include parametric amplification [38–41] and the demonstration of the dynamical Casimir effect in a Josephson metamaterial [42]. Other applications include tunable impedance matching [43] and a tunable filter [44].

With more sophisticated engineering, SQUID meta-atoms can be reduced further in size to the limit where the microscopic quantum theory applies, thus becoming qubits. In this case the qubits have a transition between their ground state and first excited state that corresponds to the absorption or emission of a single microwave photon. A collection of these qubits, interacting either directly or indirectly through a common microwave resonator, can create a quantum metamaterial with new collective properties [11,45]. Predicted properties include a superradiant state in which all of the qubits start in the excited state and are triggered to emit in phase when a single photon passes by [46]. A recent experimental result is the development of a topological edge state in a one-dimensional superconducting quantum metamaterial [47].

Superconducting metamaterials based on the Josephson effect are not limited to the SQUID architecture. In particular, a novel Josephson dielectric metamaterial with an electronically tunable plasma frequency has been demonstrated [48]. This design could be useful for a tunable plasmonic haloscope to detect candidate axionic dark matter particles [49].

All of the superconducting metamaterials discussed above display strong signatures of nonlinearity [50–54], even to the single-photon limit. Here we are interested in characterizing and understanding the nonlinear properties of individual rf SQUIDs, which can help inform the behavior of metamaterials made up of such objects. In particular, we look at the case of two equal-amplitude input microwave tones and the generation of third-order intermodulation products at nearby frequencies. Intermodulation distortion (IMD) arises from nonlinear properties of the rf SQUIDs, resulting in a mixing of the two input frequencies [55]. Intermodulation distortion generation has been widely used to characterize nonlinear systems [56,57] and superconducting materials [58–63] and devices [64–70]. When two tones at frequencies f_1 and f_2 are applied at a frequency separation $\Delta f \equiv |f_2 - f_1| \ll f_1, f_2$, third-order tones appear at frequencies Δf above and below the two input tones. Measuring such tones with a spectrum analyzer is relatively simple, and the dependence of their amplitude on the microscopic properties of the SQUIDs and metamaterial structure directly probes the nonlinear Josephson physics of these materials. Intermodulation is also of

concern in communications applications because mixing of two or more tones (in an amplifier or filter, for example) can create new tones in the bandwidth of the receiver chain and produce false signals that mimic the presence of additional users. The use of two unequal tones applied to rf SQUID metamaterials makes use of the parametric amplification effect to transfer energy from a pump tone to a signal tone. Such experiments have been very successful at producing low-noise amplification of microwave signals [41,71]. Parametric Josephson amplification shows promise for quantum-limited noise performance [72], suggesting that rf SQUID metamaterials can be a promising medium for low-noise signal processing of quantum devices [41]. These conditions are very different from those utilized here and will not be considered further. Alternatively, one could also measure harmonic generation under single-tone input. However, the properties of the metamaterial and the microwave apparatus are very different at the harmonic frequencies, making such measurements difficult to interpret.

Previous work on two-equal-amplitude-tone excitation of rf SQUIDs concentrated on how the third-order IMD amplitude depends on temperature, the rf flux drive amplitude, and the center frequency of the two driving tones [55]. That study showed a dramatic onset of IMD as a function of increasing center frequency with a strong response peak, followed by a significant dip. A second peak also occurred under high applied rf flux, creating a gap in the intermodulation (IM) response. The sharp onset was associated with the resonant response of the rf SQUID meta-atom, and the resonance tunes over a considerable frequency range as the rf flux amplitude is varied. The dip feature was found to be asymmetric between the upper and lower third-order intermodulation tones. Several approximate models of IMD generation from an rf SQUID were developed and showed good agreement with experimental data. However, all of that work was done in the limit of zero dc magnetic flux, which considerably simplified the problem, both experimentally and theoretically [55]. Consequently, several key physical phenomena went undiscovered in those studies and that situation is rectified here. Our objective in this paper is to extend the two-tone intermodulation study to the case of nonzero dc flux. A number of phenomena come into play in the presence of a dc flux that were not anticipated on the basis of prior work [55]. These phenomena are explored experimentally, and the key physics underlying their origin is uncovered through a combination of analytical and numerical investigations.

II. THEORY AND MODEL

All observable properties of an rf SQUID can be predicted once the gauge-invariant phase on the Josephson junction $\delta(t)$ is known as a function of time t for a given driving configuration. For example, the supercurrent through the junction is given by $I = I_c \sin[\delta(t)]$, where I_c is the critical current of the Josephson junction, and the voltage drop across the junction is given by $V = 2\pi \Phi_0 d\delta/dt$. A single rf SQUID can be treated as a resistively and capacitively shunted Josephson junction interrupting a superconducting loop with geometric inductance L_{geo} (see the circuit model in Fig. 1). A resistance R represents dissipative quasiparticle tunneling through the

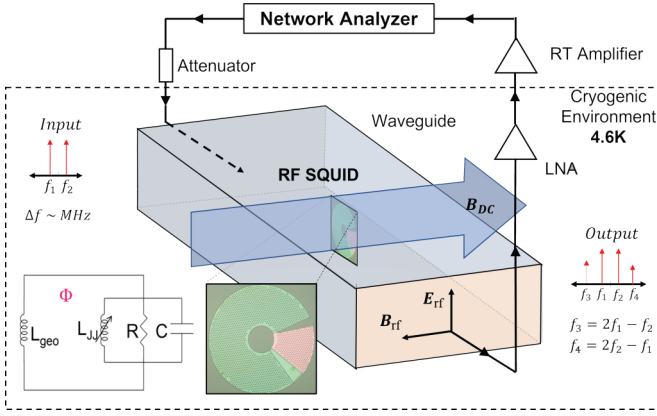


FIG. 1. Schematic of the experimental setup for intermodulation measurements of single rf SQUID meta-atoms. A microwave network analyzer at room temperature generates two equal-amplitude signals and sends them to a waveguide inside a cryogenic refrigerator at 4.6 K. The signals interact with the rf SQUID meta-atom (by applying an rf magnetic flux) and produce intermodulation products which are amplified with a cryogenic low-noise amplifier (LNA) and room temperature (RT) amplifier, before returning to the network analyzer for measurement. A perpendicular dc magnetic field can also be introduced onto the meta-atom (creating a dc magnetic flux bias) through a superconducting coil attached to the normal metal waveguide. Lower left insets show an electrical schematic of the rf SQUID, as well as an optical micrograph of one such SQUID. Upper left and lower right insets show the naming convention for the two input tones and the four output tones that are subsequently measured.

junction. Note that in this experiment the rf SQUID is designed to be nonhysteretic ($\beta_{\text{rf}} = 2\pi L_{\text{geo}} I_c / \Phi_0 < 1$).

The time evolution of the gauge-invariant phase for a driven rf SQUID described by the circuit model shown in Fig. 1 can be reduced to the dimensionless form [16,26,55]

$$\frac{d^2\delta}{d\tau^2} + \frac{1}{Q} \frac{d\delta}{d\tau} + \delta + \beta_{\text{rf}} \sin \delta = 2\pi [f_{\text{dc}} + f_{\text{rf}}(\tau)], \quad (1)$$

where $\tau = \omega_{\text{geo}} t$, $\omega_{\text{geo}} = 2\pi f_{\text{geo}} = 1/\sqrt{L_{\text{geo}} C}$ is the geometric resonant angular frequency of the rf SQUID in the absence of the Josephson effect, $Q = R\sqrt{C/L_{\text{geo}}}$ is the rf SQUID quality factor, and $f_{\text{dc}} = \Phi_{\text{dc}}/\Phi_0$ and $f_{\text{rf}} = \Phi_{\text{rf}}/\Phi_0$ are the normalized dc and rf magnetic fluxes. Note that the dimensionless parameter β_{rf} controls the strength of the nonlinearity.

The two-tone excitation of the rf SQUID can be written as $f_{\text{rf}}(\tau) = f_{\text{rf},1} \sin(\Omega_1 \tau + \theta_1) + f_{\text{rf},2} \sin(\Omega_2 \tau + \theta_2)$, where $\Omega_{1,2} = f_{1,2}/f_{\text{geo}}$ and f_1 and f_2 are the linear frequencies of the two injected tones. Here we consider the general case in which the amplitudes and phases of the driving tones are different. The dimensionless driving flux is more conveniently expressed in terms of a complex phasor envelope modulated by the central driving frequency [55]

$$f_{\text{rf}}(\tau) = \text{Re}[e^{i\Omega\tau - i\pi/2} \tilde{f}_{\text{rf}}(\tau)], \quad (2)$$

where the complex envelope function $\tilde{f}_{\text{rf}}(\tau) = f_{\text{rf},1} \exp(-i\Delta\Omega\tau/2 + i\theta_1) + f_{\text{rf},2} \exp(+i\Delta\Omega\tau/2 + i\theta_2)$, the central driving frequency $\Omega = (\Omega_1 + \Omega_2)/2$, and the difference frequency $\Delta\Omega = \Omega_2 - \Omega_1 > 0$. In the case $\Delta\Omega \ll \Omega$, the relative phase between central and difference

frequency components does not affect the solution. Thus we may disregard θ_1 and θ_2 by shifting the relative times of the central and difference frequency components [55].

Next we discuss the steady-state analytical model for the approximate solution for $\delta(\tau)$ under two-tone driving where the envelope varies so slowly that its derivatives vanish [55]. This model begins with the formulation of an ansatz solution

$$\delta(\tau) = \bar{\delta} + \tilde{\delta} \sin(\Omega\tau + \theta), \quad (3)$$

where $\bar{\delta}$ is the quasi-dc offset that will change with the slowly varying envelope \tilde{f}_{rf} , $\tilde{\delta}$ refers to the envelope of $\delta(\tau)$, and θ is the phase of $\delta(\tau)$. In general, all three variables $\bar{\delta}$, $\tilde{\delta}$, and θ have parametric time dependence through the slowly varying envelope of the rf drive at the difference frequency $\Delta\Omega$. In substituting the ansatz (3) into Eq. (1), the nonlinear term produces $\sin[\bar{\delta} + \tilde{\delta} \sin(\Omega\tau + \theta)]$, which is expanded into harmonic orders ($n\Omega$ for integer n) using the Jacobi-Anger expansion. A key approximation is that the higher-order harmonics $n > 1$ are excluded since they are substantially suppressed by the second derivative term in Eq. (1). This results in $\sin \delta \approx \sin \bar{\delta} J_0(\tilde{\delta}) + 2 \cos \bar{\delta} J_1(\tilde{\delta}) \sin(\Omega\tau + \theta)$, where J_0 and J_1 are the Bessel functions. The equation can be separated into three coupled equations for three unknowns ($\bar{\delta}$, $\tilde{\delta}$, and θ) [55]

$$(1 - \Omega^2)\bar{\delta} + 2\beta_{\text{rf}} \cos \bar{\delta} J_1(\tilde{\delta}) = 2\pi \tilde{f}_{\text{rf}} \cos \theta, \quad (4)$$

$$\frac{\Omega}{Q} \tilde{\delta} = -2\pi \tilde{f}_{\text{rf}} \sin \theta, \quad (5)$$

$$\bar{\delta} + \beta_{\text{rf}} \sin \bar{\delta} J_0(\tilde{\delta}) = 2\pi f_{\text{dc}}. \quad (6)$$

Finally, $\delta(\tau)$ can then be constructed by solving Eqs. (4)–(6) for $\bar{\delta}$, $\tilde{\delta}$, and θ for given driving flux \tilde{f}_{rf} and f_{dc} [55]. Looking forward, this model is crucial in interpreting the IMD resonant response and accurately predicts a bifurcation of the resonance frequency tuning curve with dc flux f_{dc} . It also aids in explaining the strong generation of IMD products near geometric resonance ω_{geo} . These experimentally observed features will be presented below.

III. EXPERIMENT

The experiments are carried out utilizing single rf SQUID meta-atoms. The meta-atoms were fabricated using the HYPRES $0.3\text{-}\mu\text{A}/\mu\text{m}^2$ Nb/AIO_x/Nb trilayer junction process on silicon substrates, and the meta-atom has a superconducting transition temperature $T_c = 9.2$ K [16]. An electrical schematic and optical micrograph of the rf SQUID are shown in Fig. 1. The inner radius of the rf SQUID sample is $100 \mu\text{m}$ with a geometrical area $A_0 = 31416 \mu\text{m}^2$. The effective area is estimated to increase by a factor 1.1 in comparison to the geometrical area of the rf SQUID loop due to flux focusing created by the surrounding superconducting ring ($A = 1.1A_0$). The two Nb films (135 and 300 nm thick) are connected by means of a superconducting Nb via and a Josephson junction to create a superconducting loop with geometrical inductance L_{geo} . The capacitance C has two parts: the overlap between two layers of Nb with a 200-nm-thick SiO₂ dielectric in between and the Josephson junction intrinsic capacitance. Parameter values for a typical

rf SQUID include critical current $I_c = 1.15 \mu\text{A}$, geometrical inductance $L_{\text{geo}} = 280 \text{ pH}$, zero-bias Josephson inductance $L_{\text{JJ},0} = \frac{\Phi_0}{2\pi I_c} = 286 \text{ pH}$, resistance $R = 1780 \Omega$, total capacitance $C = 0.495 \text{ pF}$, geometrical resonant frequency $f_{\text{geo}} = 13.52 \text{ GHz}$, and $\beta_{\text{rf}} = L_{\text{geo}}/L_{\text{JJ},0} = 2\pi L_{\text{geo}}I_c/\Phi_0 = 0.98$, with all temperature-dependent quantities taken at 4.6 K, below T_c .

In the experimental setup shown in Fig. 1, the rf SQUID sits in a normal metal Ku-band rectangular waveguide oriented so that the rf magnetic field of the propagating lowest-order TE mode is perpendicular to the rf SQUID. This propagating mode is used to both measure the rf SQUID response and apply a finite (and controllable) rf flux f_{rf} to the SQUID. The magnetic field of the propagating mode couples to the rf SQUID with coupling coefficient g ($g \approx 0.015$) and the resulting powers from the waveguide are amplified by 55 dB, as in the experiment [55]. Before each two-tone experiment, a single-tone transmission experiment is conducted to determine the resonant frequency at which the system has maximum power absorption. Intermodulation products are then measured systematically around the resonance; two signals of frequencies f_1 and f_2 having the same amplitude $f_{\text{rf},1} = f_{\text{rf},2}$ and a small difference in frequency $\Delta f = f_2 - f_1 > 0$ are created by the network analyzer, attenuated, and injected into the waveguide, before reaching the sample. We operate in the regime in which the rf flux amplitude applied to the SQUID is much less than a single flux quantum. The output signal contains the two main tones and their harmonics, as well as intermodulation products. The set of four tones arising from the input tones and third-order IMD is measured in the network analyzer after it has been amplified by both cryogenic and room temperature amplifiers. Note that only the magnitude, but not the phase, of each of the tones is measured. Throughout this paper we use the notation shown in Fig. 1 in which the lower third-order sideband is defined $f_3 = 2f_1 - f_2$ and the upper third-order sideband is defined $f_4 = 2f_2 - f_1$. The metamaterial exhibits strong intermodulation generation above the noise floor when superconducting (measured at $T = 4.6 \text{ K}$) and has no observable IM response at temperature above the transition temperature $T_c = 9.2 \text{ K}$. For the results discussed in this paper, in both the experiment and simulations, the following common parameters are used: $\Delta f = 10 \text{ MHz}$, $\beta_{\text{rf}} = 0.98$, $Q = 75$, and $f_{\text{geo}} = 13.52 \text{ GHz}$.

IV. NUMERICAL SIMULATIONS

In some cases, we solve the full equation of motion for $\delta(t)$ [Eq. (1)] numerically using the LSODA solver built into the FORTRAN77 library ODEPACK. To perform scans of frequency or scans of rf flux amplitude, we first find a steady-state solution with initial conditions $(\delta(0), \frac{d\delta}{dt}(0)) = (0, 0)$. The solution is considered steady once calculated over a sufficiently long time such that frequency peaks f_1 and f_2 in the Fourier transform of the time series are easily distinguished. For the parameter space examined in this paper, 20 beat periods was sufficient. In continuing the scan, the ending conditions of the previous solution seed the next solution's initial conditions. In each solution, the amplitudes δ_i of the calculated $\delta(\tau)$ corresponding to frequency components f_i are extracted via a Fourier transform ($i = 1, 2, 3, 4$). Each δ_i relates to the magnetic flux in the SQUID by $\delta_i = 2\pi(\Phi_i/\Phi_0)$. The mag-

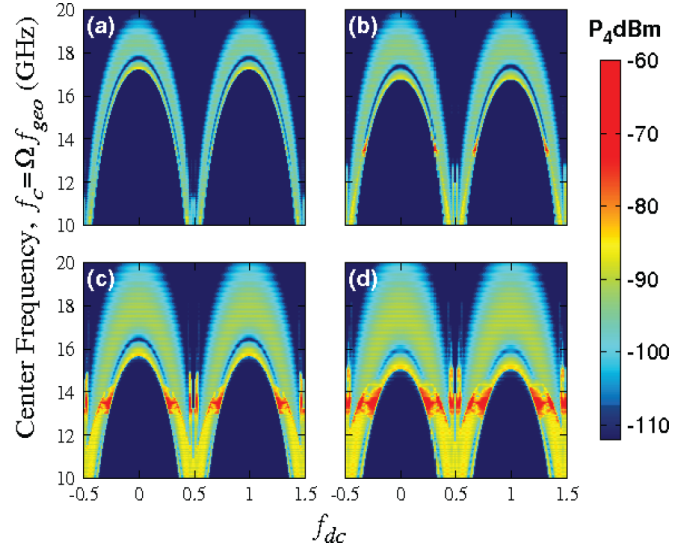


FIG. 2. Numerical simulation data for IM product P_4 (colors) vs center frequency ($f_c = \Omega f_{\text{geo}}$) and dc flux (f_{dc}) at progressively increasing f_{rf} values: (a) $f_{\text{rf}} = 10^{-1.74}$, (b) $f_{\text{rf}} = 10^{-1.49}$, (c) $f_{\text{rf}} = 10^{-1.34}$, and (d) $f_{\text{rf}} = 10^{-1.24}$. Note that f_{dc} values range from -0.5 to $+1.5$ and a common scale bar is used for the P_4 colors on all plots. Additional parameters are the same as in Fig. 3

netic flux corresponds to a magnetic field inside the single rf SQUID loop by $B_i = \Phi_i/A$, where A is the effective area of loop. The final numerically simulated powers P_{1-4} are calculated and presented for direct comparison to experiment.

The results for the intermodulation power P_4 , shown in Fig. 2, have been obtained through the following procedure. For each point on the $f_{\text{dc}}-f_c$ plane, Eq. (1) is integrated in time using the standard fourth-order Runge-Kutta algorithm with fixed time step $h = 0.02$ for 100 000 time units and the data are discarded. Then Eq. (1) is integrated further in time and a time series of $N_{\text{FT}} = 2^{22}$ values of $\delta(\tau)$ is collected every 0.1 time units which span a time interval of $\delta\tau = 419432$ time units. That time interval is much larger than the longest period of the rf SQUID dynamics, $2\pi/\Delta\Omega/2 \simeq 16990$, and includes ~ 25 such periods. The time series is then Fourier transformed and the corresponding δ_i are obtained. Note that neighboring Fourier frequencies are separated by $1/\delta\tau \simeq 2.4 \times 10^{-6}$, which allows the extraction of δ_i with high accuracy. The intermodulation power P_4 are calculated and converted to dBm using the extracted δ_4 and applying the procedure discussed above. Then the intermodulation power P_4 in dBm is mapped onto the $f_{\text{dc}}-f_c$ plane in Fig. 2 for four values of f_{rf} .

The dynamics of the rf SQUID can become chaotic in certain areas of the parameter spaces. In order to distinguish chaotic from nonchaotic states of the rf SQUID in the numerical simulations, we calculate the Lyapunov exponents, the most reliable diagnostic tool for that purpose. First, Eq. (1) is written as a system of three first-order differential equations, where besides δ and $\dot{\delta}$ time is being treated also as a dependent variable. Thus, the system of three equations is autonomous and the algorithm developed by Wolf *et al.* [73] can be employed. For the autonomous first-order system, there are three Lyapunov exponents whose sum is always $-1/Q$, a quantity that quantifies loss in the rf SQUID, while one of

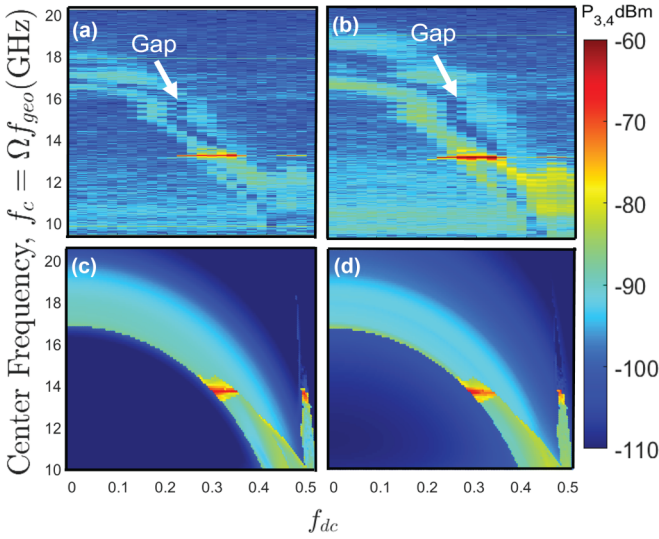


FIG. 3. Intermodulation powers P_3 and P_4 (colors) as a function of center frequency of the two input tones $f_c = \Omega f_{\text{geo}} = \frac{f_1 + f_2}{2}$ vs normalized dc flux f_{dc} from 0 to $\frac{1}{2}$ at normalized rf flux $f_{\text{rf}} = 10^{-1.49}$ at a temperature of 4.6 K. The experimental data are shown for (a) the lower (P_3) and (b) the upper (P_4) third-order IM. Similarly, a corresponding numerical simulation is shown for (c) the lower and (d) the upper third-order IM. Note that the results in (a) and (b) are horizontally translated to account for trapped flux inside the rf SQUID and/or the superconducting magnet. The coloring refers to the power of IM response in dBm as measured or simulated from a Ku band waveguide and a single common color bar is used for all plots. Prominent gaps in experimental IM response are pointed out in (a) and (b). Corresponding gaps in the simulations are illustrated in Fig. 6. The simulation parameters are $\Delta f = 10$ MHz, $\beta_{\text{rf}} = 0.98$, $Q = 75$, and $f_{\text{geo}} = 13.52$ GHz.

them is always zero. The necessary time integration of the combined system of the three first-order equations and their variational equations is performed by a Runge-Kutta fourth-order algorithm with constant time step, typically $h = 0.01$. The maximum Lyapunov exponent λ_{max} is then mapped on part of the $f_{\text{dc}}-f_c$ plane in Fig. 9(b), which determines whether the rf SQUID is in a chaotic state ($\lambda_{\text{max}} > 0$) or not ($\lambda_{\text{max}} \leq 0$). The time allowed for the Lyapunov exponents to relax to an almost constant value is more than 500 000 time units. Compared with the longest period of the rf SQUID dynamics, $2\pi/\Delta\Omega/2 \simeq 16\,990$, that time interval includes more than 30 of these periods.

V. RESULTS

We first give an overview of the IMD data as a function of input tone center frequency and dc flux. Figures 3(a) and 3(b) show the measured lower (P_3) and upper (P_4) third-order intermodulation strengths as a function of center frequency (from 10 to 20 GHz) of the two input tones (vertical axis) and dc magnetic flux in the range from 0 to $\Phi_0/2$ ($0 \leq f_{\text{dc}} \leq \frac{1}{2}$). We define the center driving frequency as $f_c = \Omega f_{\text{geo}}$. For a given value of f_{dc} we note that as a function of increasing center frequency there is a resonant onset of IMD, illustrated as a sharp transition from dark blue to light blue. The dc magnetic flux tunes the resonant onset frequency of the rf SQUID in a

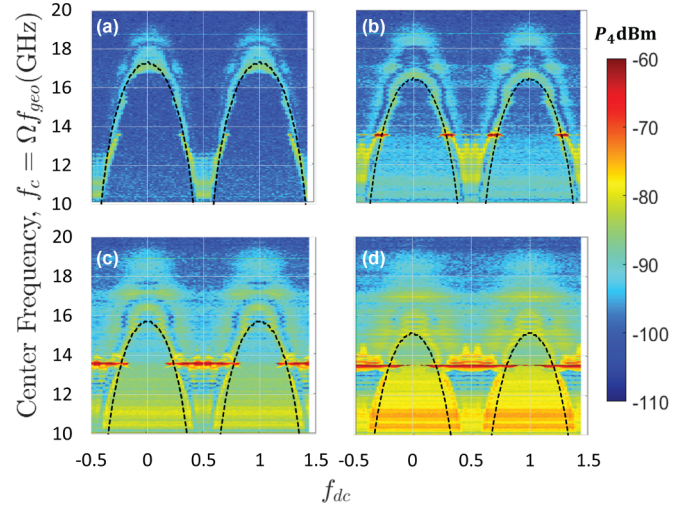


FIG. 4. Experimental data for IM product P_4 (colors) vs center frequency (Ωf_{geo}) and dc flux (f_{dc}) at progressively increasing f_{rf} values: (a) $f_{\text{rf}} = 10^{-1.74}$, (b) $f_{\text{rf}} = 10^{-1.49}$, (c) $f_{\text{rf}} = 10^{-1.34}$, and (d) $f_{\text{rf}} = 10^{-1.24}$. Note that f_{dc} values range from -0.5 to $+1.5$ and the data are taken at a temperature of $T = 4.6$ K. The black dashed curves correspond to the analytically derived resonance frequency vs f_{dc} evolution using the steady-state model discussed in the text. A common scale bar is used for the P_4 colors on all plots. Additional parameters are the same as in Fig. 3.

periodic manner, with period Φ_0 (only the first half is shown in Fig. 3, but two periods are shown in Fig. 4). This is the first demonstration of dc flux dependence of resonant response for f_{rf} in the nonlinear region ($10^{-3} < f_{\text{rf}} < 10^{-1}$). We note that the tuning of resonant frequency, as well as the strong IMD response, is qualitatively similar to that previously seen as a function of rf flux amplitude in zero dc flux (see Fig. 2 of Ref. [55]). In Figs. 3(c) and 3(d), numerical simulations for the dc flux dependence of the lower and the upper third-order IMD (P_3 and P_4) show features similar to the experimental data. We note that the data and simulation results for P_3 and P_4 in Fig. 3 are plotted on a common color bar and the results show many common features. These include the asymmetry of response between P_3 and P_4 .

Figure 4 shows that the tuning of the P_4 IMD resonant response with dc flux f_{dc} is expected to be periodic in units of the flux quantum Φ_0 . This figure also illustrates the changes in rf SQUID IM as the rf flux amplitude f_{rf} is varied through progressively higher values in the nonlinear rf response regime. We note that the frequency tuning range of IM is reduced with increasing f_{rf} , and strong IM begins to develop near the geometrical resonance frequency of the rf SQUID f_{geo} . Figure 2 shows numerical solutions for P_4 for the corresponding experimental conditions shown in Fig. 4. A number of features are reproduced from the data, including the strong onset of IM generation with increasing center frequency f_c at fixed dc flux f_{dc} , a clear gap in P_4 above the onset, and increased generation of IM near the geometrical resonance frequency with increased rf flux f_{rf} .

From these results, three dominant features characterize the IMD response: (A) the resonant frequency tuning with dc flux, (B) a gap in P_4 response above the tuning curve as a func-

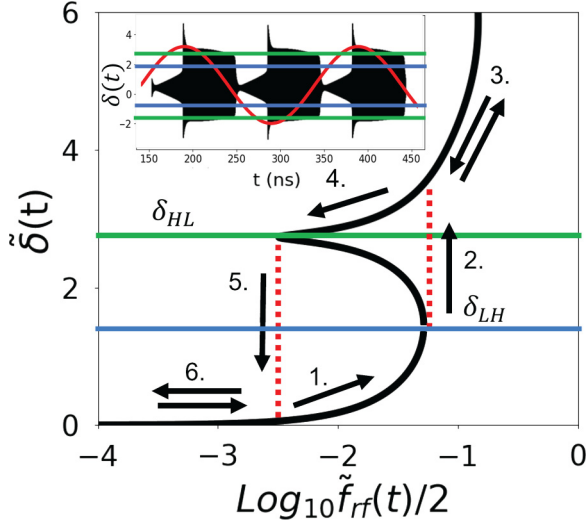


FIG. 5. Illustration of the bistability in $\tilde{\delta}$ using the steady-state model. The black curve shows a representative solution to Eqs. (4)–(6) for $\tilde{\delta}$ vs \tilde{f}_{rf} for a given f_{dc} . The numbered arrows describe the transitions of the time-dependent envelope $\tilde{\delta}(t)$. The inset shows the resulting time dependence of $\delta(t)$ (black). The red curve displays $\tilde{f}_{rf}(t)$ scaled vertically to fit the figure. The horizontal blue and green lines correspond to those in the main figure.

tion of frequency (or dc flux), and (C) a sharp enhancement of IM output power as the tuning curve crosses the geometric resonance ($f_{geo} = 13.52$ GHz). Each of these features in the experimental data will be addressed in more detail below and compared to analytical and numerical modeling.

A. IMD resonant frequency tuning

First we will examine the tuning of the rf SQUID resonant response with respect to dc flux, at various rf flux amplitudes, as illustrated in Fig. 4. In the low rf flux limit ($f_{rf} < 10^{-3}$), the analytical linear-response model predicts that the single SQUID resonance frequency tunes from $f_{geo}\sqrt{1 + \beta_{rf}}$ when $f_{dc} = n$ to $f_{geo}\sqrt{1 - \beta_{rf}}$ when $f_{dc} = n/2$, for all positive and negative integers n , including zero (here we assume $\beta_{rf} < 1$) [21]. Using the steady-state analytical model (outlined above), this concept of resonance can be extended to the IM response. In this framework, one can define IM resonance in terms of the bistable transition in the envelope of the gauge-invariant phase difference $\tilde{\delta}(\tau)$. The model shows that there is a large increase in P_3 and P_4 when $\tilde{\delta}(\tau)$ undergoes a bistable transition. In solving the system of equations (4)–(6) using a constant f_{dc} , a solution curve for $\tilde{\delta}$ vs \tilde{f}_{rf} is constructed, as illustrated in Fig. 5. The thick black curve relates the envelope of the gauge-invariant phase difference $\tilde{\delta}$ to the envelope of the two-tone driving rf flux \tilde{f}_{rf} , which are both time dependent on the scale of the difference frequency $\Delta\Omega$. (Note that the horizontal axis of this plot is on a logarithmic scale of $\tilde{f}_{rf}/2$. Since the rf drive consists of two equal-amplitude tones, $\tilde{f}_{rf}/2$ thus corresponds to the power of one of the two tones.)

Bistable transitions in $\tilde{\delta}$ can be described by a cycle over the course of half a beat period in \tilde{f}_{rf} . In reference to Fig. 5, let the cycle begin at $\tilde{f}_{rf} = 0$ and consider increasing \tilde{f}_{rf} . (1) $\tilde{\delta}$ will increase on the lowest branch of the black line as \tilde{f}_{rf} increases

until $\tilde{\delta}$ is equal to δ_{LH} (horizontal blue line in Fig. 5). (2) $\tilde{\delta}$ is faced with a crisis and transitions to the next higher branch. (3) $\tilde{\delta}$ will increase on this upper branch until \tilde{f}_{rf} reaches its maximum value. (4) $\tilde{\delta}$ will decrease on the higher branch as \tilde{f}_{rf} decreases until $\tilde{\delta}$ is equal to δ_{HL} (horizontal green line in Fig. 5). (5) $\tilde{\delta}$ is faced with another crisis and transitions to the lower branch. (6) $\tilde{\delta}$ continues to decrease as \tilde{f}_{rf} decreases until passing $\tilde{f}_{rf} = 0$ and repeating the cycle for negative \tilde{f}_{rf} . This results in two (hysteretic) transitions in $\tilde{\delta}$ per cycle of \tilde{f}_{rf} as seen in the inset plot of $\delta(t)$ in Fig. 5. In reference to this cycle, we define IMD resonance as the point where the maximum of \tilde{f}_{rf} coincides with the initial crisis transition such that step 3 begins to occur. In Fig. 5 this would occur at $\log_{10}(\tilde{f}_{rf}/2) \approx -1.2$.

The inset in Fig. 5 shows the resulting waveform of $\delta(t)$, in which the bistable transitions in the envelope $\tilde{\delta}(t)$ result in large IMD production. Note that these curves may have several crisis locations resulting in multiple bistable transitions over one half beat of rf flux and result in prolific production of IMD.

Analytically derived tuning curves in f_c vs f_{dc} can be constructed by increasing the frequency used in the steady-state analytical model until the condition for resonance to occur (described above) is satisfied. The frequency at which this condition occurs for a given f_{rf} and f_{dc} is defined as the IM resonant frequency. The resonance frequency can be determined for varying f_{dc} , resulting in tuning curves in f_c vs f_{dc} . Figures 4(a)–4(d) show these analytically derived curves as dashed lines which are superimposed on experimental results taken at corresponding f_{rf} levels. Note that the IM resonance in this context corresponds to the onset of strong IM response from the transitions between different solution branches, rather than a peak in the response. Thus, a strong IM response should be found near but not exactly at this resonance. There is good agreement between the experimental data and model with regard to IMD resonant frequency tuning. Specifically, as f_{rf} increases, the frequency range of IMD resonance tuning by means of dc flux is reduced. This is most apparent when observing how the resonant frequency at $f_{dc} = n$ approaches f_{geo} as f_{rf} increases. To further solidify this point we utilize full numerical solutions to the rf SQUID equation of motion [Eq. (1)] under the same conditions as the data in Fig. 4, and the results are shown in Fig. 2. We find excellent agreement between the experimental and the numerical results in terms of the dc flux tuning of IMD resonance with varying f_{rf} .

B. Gaps in IMD power

We next discuss the IMD gap above resonance evident in the data in Figs. 3 and 4. In the zero dc flux limit, a gap in IMD was observed above the resonance frequency [55]. Figures 3 and 4 show that this gap continuously tracks with the resonance frequency tuning curve, creating a segment of low IMD response. The numerical results for $P_4(f_c, f_{dc})$ in Fig. 2 parallel the data shown in Fig. 4. Here the gaps are quite prominent and display a different character above and below the geometric resonance frequency $f_{geo} = 13.52$ GHz, similar to the data. Figure 6 shows these gaps explicitly by taking horizontal (constant frequency f_c) cuts of numerical results

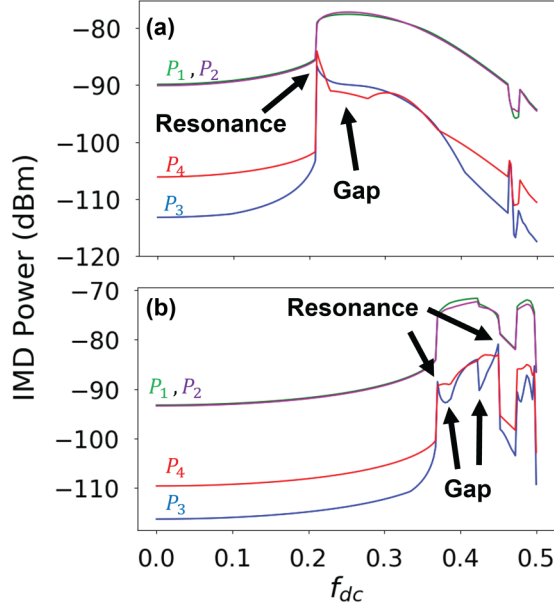


FIG. 6. Fundamental input (P_1 and P_2) and IM output (P_3 and P_4) power (dBm) vs dc flux f_{dc} , illustrating gaps in both the lower and the upper third-order IM. Horizontal constant frequency line cuts from numerical simulations presented in Figs. 3(c) and 3(d) are shown at constant center driving frequencies (a) $f_c = 1.11f_{\text{geo}} = 15$ GHz and (b) $f_c = 0.81f_{\text{geo}} = 11$ GHz.

in Figs. 3(c) and 3(d). The gap traces out the tuning curve such that it exists in both the frequency (f_c) and dc flux (f_{dc}) domains. Figure 6(a) shows this gap above resonance in dc flux for a constant center frequency $f_c = 1.11f_{\text{geo}} = 15$ GHz, while Fig. 6(b) is a line cut taken at $f_c = 0.88f_{\text{geo}} = 12$ GHz. Within each gap, there is an asymmetry between P_3 and P_4 : When $f > f_{\text{geo}}$, $P_4 < P_3$, and when $f < f_{\text{geo}}$, $P_4 > P_3$. In addition to the gap immediately following resonance in Fig. 6(b) there is a secondary gap at larger dc flux $f_{dc} \approx 0.42$. The gap is particularly clear in the numerical simulation shown in Fig. 2. As f_{rf} increases to the nonlinear regime, a gap below f_{geo} develops and becomes more distinct. This is in qualitative agreement with data shown in Fig. 4. Further details about the origin and asymmetry of the gaps in P_3 and P_4 are discussed in our previous work [55,74].

C. Enhancement of IMD near the geometric resonant frequency f_{geo}

It is clear from the data in Figs. 3 and 4 that for certain ranges of f_{dc} there is an enhanced IMD response for drive center frequencies f_c near $f_{\text{geo}} = 13.52$ GHz. This enhancement is hardly surprising since extreme multistability near f_{geo} has been modeled and observed before, albeit at $f_{dc} = 0$ [19]. To investigate further, we examine the strong enhancement in IMD power for f_c close to f_{geo} , as a function of f_{rf} and f_{dc} , as shown in Figs. 7(a) (data) and 7(b) (simulation). In this case we choose a center frequency $f_c = 0.998f_{\text{geo}} = 13.49$ GHz, just below the geometric resonant frequency. Little difference was observed between P_3 and P_4 in regard to the following discussion, so only P_4 is considered. In addition, there was minimal hysteresis in the rf flux sweep with two-equal-

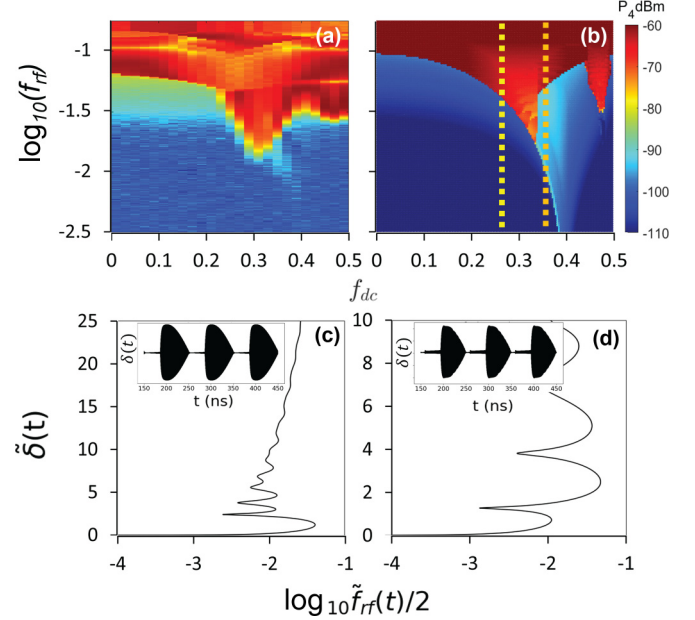


FIG. 7. (a) Experimental data and (b) numerical simulation for the upper third IM power P_4 (shown on a common color bar in dBm) as a function of f_{rf} and f_{dc} , taken at $f_c = 0.999f_{\text{geo}} = 13.50$ GHz while sweeping f_{rf} from low to high. (c) Solutions to Eqs. (4)–(6) for $\tilde{\delta}$ vs \tilde{f}_{rf} at $f_{dc} = 0.25$ when $f_{\text{rf}} \approx 10^{-1.3}$. This case corresponds to the left vertical yellow line in (b). The inset shows $\delta(t)$ at $f_{\text{rf}} = 10^{-1.3}$. (d) Solutions to Eqs. (4)–(6) at $f_{dc} = 0.35$ when $f_{\text{rf}} \approx 10^{-1.3}$. This case corresponds to the right vertical orange line in (b). The inset shows $\delta(t)$ at $f_{\text{rf}} = 10^{-1.3}$.

amplitude stimulation [55]. Thus, only the low to high rf flux sweeps are shown. There are three common features worth noting between the experiment and the simulation shown in Fig. 7.

The first feature is the main IMD resonance tuning curve, which extends from approximately $f_{\text{rf}} = 10^{-1}$ at $f_{dc} = 0$ to $f_{\text{rf}} < 10^{-2.5}$ at $f_{dc} = 0.4$ in Fig. 7(b). This curve represents the IMD resonance condition in $f_{\text{rf}}-f_{dc}$ space for $f_c = 0.998f_{\text{geo}} = 13.49$ GHz. As f_{rf} is increased across this resonance curve, a massive increase in IMD production of approximately 40 dB can be observed. Note that the data in Fig. 7(a) show evidence of the same tuning curve, with a trace of the transition continuing beneath the “tooth” of IMD response centered at $f_{dc} \approx 0.3$. The mechanism underlying the appearance of this tooth will be discussed next.

The second common feature between the experiment and the simulation is the bifurcation of the IMD resonance tuning curve near $f_{dc} = 0.3$. Its origin can be qualitatively understood through the steady-state analytical model. Figures 7(c) and 7(d) show the $\tilde{\delta}-\tilde{f}_{\text{rf}}$ solution curves from the steady-state model for two values of f_{dc} before and after the bifurcation. In Fig. 7(c), where $f_{dc} = 0.25$ is below the f_{dc} value for the onset of bifurcation, we can see that for any $f_{\text{rf}} \gtrsim 10^{-1.4}$ a bistable transition would occur and this transition increases $\tilde{\delta}$ by an order of magnitude. On the other hand, in Fig. 7(d), where $f_{dc} = 0.35$ is above the value for the onset of bifurcation, two transitions may occur, with one at $\tilde{f}_{\text{rf}}/2 \approx 10^{-1.9}$ corresponding to the lower resonance in Figs. 7(a) and 7(b) and another

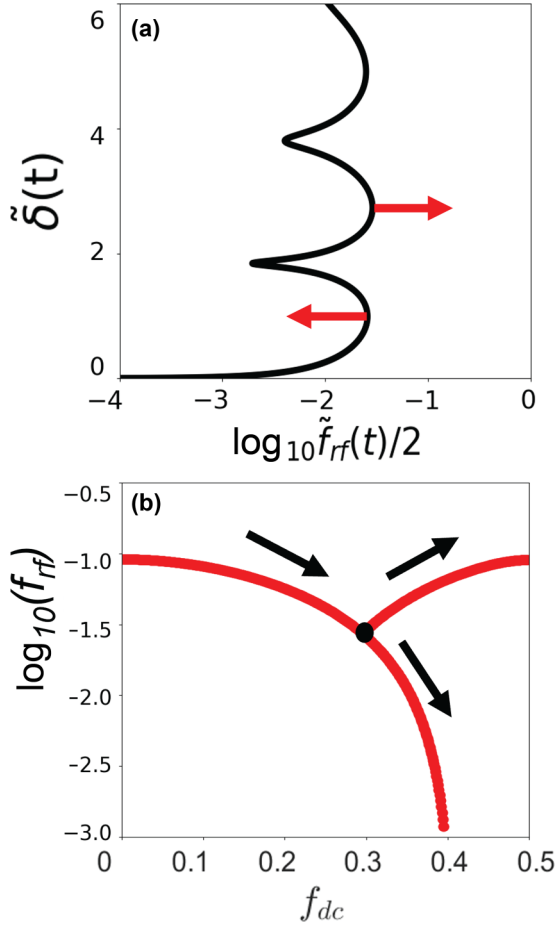


FIG. 8. Illustration of the bifurcation of resonance frequency according to the steady-state analytical model. At $f_c = 0.998f_{\text{geo}} = 13.49$ GHz, resonance bifurcation begins at $f_{\text{dc}} = 0.3$. (a) Solution for $\tilde{\delta}$ vs \tilde{f}_{rf} for $f_{\text{dc}} = 0.3$. Red arrows indicate the movement of transition peaks as f_{dc} increases. Here $f_{\text{dc}} > 0.3$ allows two transitions below $f_{\text{rf}} = 0.1$; $f_{\text{dc}} < 0.3$ allows only one. (b) Resonance in f_{rf} vs f_{dc} at $f_c = 0.998f_{\text{geo}} = 13.49$ GHz. The black dot represents the point of bifurcation shown in (a).

at $\tilde{f}_{\text{rf}}/2 \approx 10^{-1.3}$ corresponding to the higher resonance in Figs. 7(a) and 7(b). This is also observed in the inset diagram of Fig. 7(d), where the envelope of $\delta(t)$ has an initial small transition ($\Delta\tilde{\delta} \approx 1$) followed by the large secondary transition ($\Delta\tilde{\delta} \approx 40$) during a single beat. The dominating second transition also explains the much stronger IMD response above the higher resonance compared to the lower after the bifurcation.

Figure 8(a) shows the $\tilde{\delta}$ - \tilde{f}_{rf} solution curve at exactly the bifurcation point, where there are two vertically aligned crisis locations. The crisis points will move in \tilde{f}_{rf} as f_{dc} increases according to the arrows shown, such that for $f_{\text{dc}} > 0.3$ two transitions may occur as in Fig. 7(d), while for $f_{\text{dc}} < 0.3$ only one transition occurs as in Fig. 7(c). The resulting bifurcation of the IMD resonance frequency in f_{rf} vs f_{dc} can be seen in Fig. 8(b), which qualitatively reproduces the main bifurcation and the tooth of high IMD response at $f_{\text{dc}} = 0.32$ seen in the f_{rf} - f_{dc} plots in Figs. 7(a) and 7(b).

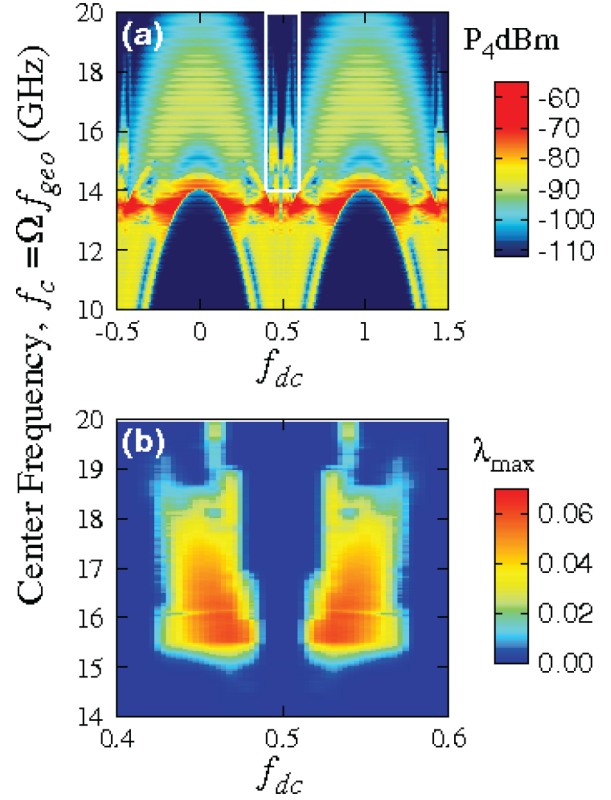


FIG. 9. (a) Numerical data for IM product P_4 (colors) vs center frequency ($f_c = \Omega f_{\text{geo}}$) and dc flux (f_{dc}) at $f_{\text{rf}} = 10^{-1.10}$. (b) Corresponding maximum Lyapunov exponent shown for the area enclosed in the white rectangle in (a). Additional parameters are the same as in Fig. 3.

The third common feature between the experiment and the simulation is the second tooth of high IMD response projecting into lower f_{rf} located at approximately $f_{\text{dc}} = 0.48$. Unlike the other two features, this tooth cannot be explained by the steady-state analytical model. It is hypothesized that the exclusion of higher-order harmonics in the steady-state model is the cause of this issue.

Some connections can be made by comparing the enhancement of IMD response seen from tuning curves in different parameter spaces. Specifically, a line cut at $f_{\text{rf}} = 10^{-1.49}$ in the f_{rf} - f_{dc} space for a constant f_c [see Figs. 7(a) and 7(b)] can be transformed into the line cut at $f_c = 0.999f_{\text{geo}} = 13.50$ GHz in f_c - f_{dc} space for a constant f_{rf} [see Figs. 3(b) and 3(d)]. As the main tuning curve passes f_{geo} in Figs. 3(b) and 3(d), it splits into two resonance branches just as the above-mentioned line cut in Figs. 7(a) and 7(b) intersects with both of the tooth structures. The lower branch has a much weaker response and gradually dissipates as f_{dc} increases to 0.5, while the upper branch is much stronger. This is seen more clearly in Fig. 6(b) when there are two resonances and two gaps for $f_{\text{dc}} < 0.48$. The resonance at $f_{\text{dc}} \approx 0.46$ corresponds to the upper branch and has a stronger response than the lower at $f_{\text{dc}} \approx 0.38$. Similarly, in Figs. 7(a) and 7(b) the line cut at $f_{\text{rf}} = 10^{-1.49}$ has a stronger response near the second tooth where $f_{\text{dc}} = 0.48$ compared to the response at the first tooth where $f_{\text{dc}} = 0.32$.

VI. DISCUSSION

There are other aspects of nonlinear dynamics that could be observed in the intermodulation measurement. Here we confine ourselves to discussing the possibility of chaos induced in the rf SQUID response by a two-tone rf drive, combined with a finite dc flux f_{dc} .

The dynamics of Eq. (1) can be chaotic in certain regions of parameter space (see [23] and references therein). The rf SQUID is mainly, for most of the external control parameter values, in a quasiperiodic state due to the two-tone quasiperiodic driving field. The distinction between the chaos and quasiperiodicity of an rf SQUID is nontrivial experimentally, but numerically possible through the calculation of the Lyapunov exponents. Let us consider the parameter space of f_{dc} vs the center frequency f_c as in Fig. 9. Our numerical simulations have revealed that chaotic states appear very close to half-integer bias flux f_{dc} , for f_c greater than the geometrical frequency $f_{geo} = 13.52$ GHz. The areas on the f_{dc} - f_c plane in which the rf SQUID is in a chaotic state grow with increasing amplitude of the external rf field f_{rf} .

In Fig. 9(a) the intermodulation power P_4 (in dBm) for $f_{rf} = 10^{-1.1}$ is mapped onto the f_{dc} - f_c parameter plane. The observed pattern exhibits characteristics similar to those observed in Fig. 2. However, due to the relatively high value of f_{rf} , the rf SQUID exhibits a strong response around the geometrical frequency f_{geo} (red features) over almost the entire range of f_{dc} values. Even for that relatively high value of f_{rf} , however, in most of the area of the f_{dc} - f_c parameter plane the rf SQUID is in a nonchaotic state.

In Fig. 9(b) the maximum Lyapunov exponent λ_{max} is mapped for part of that plane around $f_{dc} = 0.5$ [enclosed in the white rectangle in Fig. 9(a)]. In the blue areas of the map, λ_{max} is zero or just below zero, indicating that the rf SQUID is in a nonchaotic state. In the rest of the area of the plane, λ_{max} is greater than zero, indicating that the rf SQUID is in a chaotic state. Note that there are two relatively small chaotic

areas in that part of the f_{dc} - f_c plane, which are located symmetrically around $f_{dc} = 0.5$. Such chaotic areas, of similar size and shape, appear around any half-integer value of f_{dc} in the same range of frequencies. The chaotic areas shrink with decreasing f_{rf} until they practically vanish for $f_{rf} \lesssim 0.025$. It should be also noted that chaotic areas of similar shape appear on the f_{dc} - f_{rf} parameter plane which are symmetrically located around half-integer values of f_{dc} , for $f_{rf} = 0.05$ – 0.20 (not shown).

VII. CONCLUSION

We have observed the first tuning of intermodulation response with dc flux applied to a single rf SQUID meta-atom. Above the IM resonance defined in this paper, prominent gaps are observed and also tunable with a dc magnetic flux. The IM response is enhanced as the IM resonance is tuned through the geometric resonance of the SQUID. The enhanced IM response near geometric resonance also shows a bifurcation in f_{rf} - f_{dc} space. All of these features are understood in a semi-quantitative manner through a combination of a steady-state approximation model and a full numerical treatment of the rf SQUID dynamics. The numerical solutions also predict the presence of chaos in narrow parameter regimes.

ACKNOWLEDGMENTS

The work at University of Maryland was funded by the U.S. Department of Energy, Office of Basic Energy Sciences, Division of Materials Sciences and Engineering under Award DE-SC0018788. We acknowledge use of facilities at the Maryland Quantum Materials Center and the Maryland NanoCenter. J.H. and N.L. acknowledge support from the General Secretariat for Research and Technology and the Hellenic Foundation for Research and Innovation (Grant No. 203).

-
- [1] V. G. Veselago, The electrodynamics of substances with simultaneously negative values of ϵ and μ , *Sov. Phys. Usp.* **10**, 509 (1968).
 - [2] J. B. Pendry, A. J. Holden, W. J. Stewart, and I. Youngs, Extremely Low Frequency Plasmons in Metallic Mesostructures, *Phys. Rev. Lett.* **76**, 4773 (1996).
 - [3] J. B. Pendry, A. J. Holden, D. J. Robbins, and W. J. Stewart, Magnetism from conductors and enhanced nonlinear phenomena, *IEEE Trans. Microwave Theory Tech.* **47**, 2075 (1999).
 - [4] R. A. Shelby, D. R. Smith, and S. Schultz, Experimental verification of a negative index of refraction, *Science* **292**, 77 (2001).
 - [5] M. Ricci, N. Orloff, and S. M. Anlage, Superconducting metamaterials, *Appl. Phys. Lett.* **87**, 034102 (2005).
 - [6] S. M. Anlage, The physics and applications of superconducting metamaterials, *J. Opt.* **13**, 024001 (2011).
 - [7] C. Kurter, J. Abrahams, and S. M. Anlage, Miniaturized superconducting metamaterials for radio frequencies, *Appl. Phys. Lett.* **96**, 253504 (2010).
 - [8] C. Kurter, A. P. Zhuravel, J. Abrahams, C. L. Bennett, A. V. Ustinov, and S. M. Anlage, Superconducting RF metamaterials made with magnetically active planar spirals, *IEEE Trans. Appl. Supercond.* **21**, 709 (2011).
 - [9] P. Jung, A. V. Ustinov, and S. M. Anlage, Progress in superconducting metamaterials, *Supercond. Sci. Technol.* **27**, 073001 (2014).
 - [10] A. H. Silver and J. E. Zimmerman, Quantum states and transitions in weakly connected superconducting rings, *Phys. Rev.* **157**, 317 (1967).
 - [11] C. Du, H. Chen, and S. Li, Quantum left-handed metamaterial from superconducting quantum-interference devices, *Phys. Rev. B* **74**, 113105 (2006).
 - [12] N. Lazarides and G. P. Tsironis, rf superconducting quantum interference device metamaterials, *Appl. Phys. Lett.* **90**, 163501 (2007).
 - [13] N. Lazarides and G. P. Tsironis, Superconducting metamaterials, *Phys. Rep.* **752**, 1 (2018).
 - [14] P. Jung, S. Butz, S. V. Shitov, and A. V. Ustinov, Low-loss tunable metamaterials using superconducting circuits with Josephson junctions, *Appl. Phys. Lett.* **102**, 062601 (2013).

- [15] S. Butz, P. Jung, L. V. Filippenko, V. P. Koshelets, and A. V. Ustinov, A one-dimensional tunable magnetic metamaterial, *Opt. Express* **21**, 22540 (2013).
- [16] M. Trepanier, D. Zhang, O. Mukhanov, and S. M. Anlage, Realization and Modeling of Metamaterials Made of rf Superconducting Quantum-Interference Devices, *Phys. Rev. X* **3**, 041029 (2013).
- [17] N. Lazarides and G. P. Tsironis, Multistability and self-organization in disordered SQUID metamaterials, *Supercond. Sci. Technol.* **26**, 084006 (2013).
- [18] M. M. Müller, B. Maier, C. Rockstuhl, and M. Hochbruck, Analytical and numerical analysis of linear and nonlinear properties of an rf-SQUID based metasurface, *Phys. Rev. B* **99**, 075401 (2019).
- [19] P. Jung, S. Butz, M. Marthaler, M. V. Fistul, J. Leppäkangas, V. P. Koshelets, and A. V. Ustinov, Multistability and switching in a superconducting metamaterial, *Nat. Commun.* **5**, 3730 (2014).
- [20] G. P. Tsironis, N. Lazarides, and I. Margaritis, Wide-band tunability, nonlinear transmission, and dynamic multistability in SQUID metamaterials, *Appl. Phys. A* **117**, 579 (2014).
- [21] D. Zhang, M. Trepanier, O. Mukhanov, and S. M. Anlage, Tunable Broadband Transparency of Macroscopic Quantum Superconducting Metamaterials, *Phys. Rev. X* **5**, 041045 (2015).
- [22] T. Zhou, F. Moss, and A. Bulsara, Observation of a strange nonchaotic attractor in a multistable potential, *Phys. Rev. A* **45**, 5394 (1992).
- [23] J. Hizanidis, N. Lazarides, and G. P. Tsironis, Flux bias-controlled chaos and extreme multistability in SQUID oscillators, *Chaos* **28**, 063117 (2018).
- [24] J. Shena, N. Lazarides, and J. Hizanidis, Multi-branched resonances, chaos through quasiperiodicity, and asymmetric states in a superconducting dimer, *Chaos* **30**, 123127 (2020).
- [25] M. Trepanier, Tunable nonlinear superconducting metamaterials: Experiment and simulation, Ph.D. thesis, University of Maryland, 2015, <https://drum.lib.umd.edu/handle/1903/17290>.
- [26] M. Trepanier, D. Zhang, O. Mukhanov, V. P. Koshelets, P. Jung, S. Butz, E. Ott, T. M. Antonsen, A. V. Ustinov, and S. M. Anlage, Coherent oscillations of driven rf SQUID metamaterials, *Phys. Rev. E* **95**, 050201(R) (2017).
- [27] N. Lazarides and G. P. Tsironis, SQUID metamaterials on a Lieb lattice: From flat-band to nonlinear localization, *Phys. Rev. B* **96**, 054305 (2017).
- [28] N. Lazarides and G. P. Tsironis, Multistable dissipative breathers and collective states in SQUID Lieb metamaterials, *Phys. Rev. E* **98**, 012207 (2018).
- [29] P. Jung, R. Kosarev, A. Zhuravel, S. Butz, V. P. Koshelets, L. V. Filippenko, A. Karpov, and A. V. Ustinov, Imaging the electromagnetic response of superconducting metasurfaces, in *Proceedings of the Seventh International Congress on Advanced Electromagnetic Materials in Microwaves and Optics, Talence, France* (IEEE, Piscataway, 2013), pp. 283–285.
- [30] A. P. Zhuravel, S. Bae, A. V. Lukashenko, A. S. Averkin, A. V. Ustinov, and S. M. Anlage, Imaging collective behavior in an rf-SQUID metamaterial tuned by dc and rf magnetic fields, *Appl. Phys. Lett.* **114**, 082601 (2019).
- [31] N. Lazarides, G. Neofotistos, and G. P. Tsironis, Chimeras in SQUID metamaterials, *Phys. Rev. B* **91**, 054303 (2015).
- [32] J. Hizanidis, N. Lazarides, and G. P. Tsironis, Robust chimera states in SQUID metamaterials with local interactions, *Phys. Rev. E* **94**, 032219 (2016).
- [33] J. Hizanidis, N. Lazarides, G. Neofotistos, and G. Tsironis, Chimera states and synchronization in magnetically driven SQUID metamaterials, *Eur. Phys. J.: Spec. Top.* **225**, 1231 (2016).
- [34] A. Banerjee and D. Sikder, Transient chaos generates small chimeras, *Phys. Rev. E* **98**, 032220 (2018).
- [35] J. Hizanidis, N. Lazarides, and G. P. Tsironis, Chimera states in networks of locally and non-locally coupled SQUIDs, *Front. Appl. Math. Stat.* **5**, 33 (2019).
- [36] J. Hizanidis, N. Lazarides, and G. P. Tsironis, Pattern formation and chimera states in 2D SQUID metamaterials, *Chaos* **30**, 013115 (2020).
- [37] N. Lazarides, J. Hizanidis, and G. P. Tsironis, Controlled generation of chimera states in SQUID metasurfaces using dc flux gradients, *Chaos Soliton. Fractal.* **130**, 109413 (2020).
- [38] M. A. Castellanos-Beltran and K. W. Lehnert, Widely tunable parametric amplifier based on a superconducting quantum interference device array resonator, *Appl. Phys. Lett.* **91**, 083509 (2007).
- [39] M. A. Castellanos-Beltran, K. D. Irwin, G. C. Hilton, L. R. Vale, and K. W. Lehnert, Amplification and squeezing of quantum noise with a tunable Josephson metamaterial, *Nat. Phys.* **4**, 929 (2008).
- [40] C. Macklin, K. O'Brien, D. Hover, M. E. Schwartz, V. Bolkhovskiy, X. Zhang, W. D. Oliver, and I. Siddiqi, A near-quantum-limited Josephson traveling-wave parametric amplifier, *Science* **350**, 307 (2015).
- [41] E. I. Kiselev, A. S. Averkin, M. V. Fistul, V. P. Koshelets, and A. V. Ustinov, Two-tone spectroscopy of a SQUID metamaterial in the nonlinear regime, *Phys. Rev. Research* **1**, 033096 (2019).
- [42] P. Lähteenmäki, G. S. Paraoanu, J. Hassel, and P. J. Hakonen, Dynamical Casimir effect in a Josephson metamaterial, *Proc. Natl. Acad. Sci. USA* **110**, 4234 (2013).
- [43] C. Altimiras, O. Parlavacchio, P. Joyez, D. Vion, P. Roche, D. Esteve, and F. Portier, Tunable microwave impedance matching to a high impedance source using a Josephson metamaterial, *Appl. Phys. Lett.* **103**, 212601 (2013).
- [44] S. Kim, D. Shrekenhamer, K. McElroy, A. Strikwerda, and J. Alldredge, Tunable superconducting cavity using superconducting quantum interference device metamaterials, *Sci. Rep.* **9**, 4630 (2019).
- [45] P. Macha, G. Oelsner, J.-M. Reiner, M. Marthaler, S. André, G. Schön, U. Hübner, H.-G. Meyer, E. Il'ichev, and A. V. Ustinov, Implementation of a quantum metamaterial using superconducting qubits, *Nat. Commun.* **5**, 5146 (2014).
- [46] Z. Ivić, N. Lazarides, and G. P. Tsironis, Qubit lattice coherence induced by electromagnetic pulses in superconducting metamaterials, *Sci. Rep.* **6**, 29374 (2016).
- [47] I. S. Besedin, M. A. Gorlach, N. N. Abramov, I. Tsitsilin, I. N. Moskalenko, A. A. Dobronosova, D. O. Moskalev, A. R. Matanin, N. S. Smirnov, I. A. Rodionov, A. N. Poddubny, and A. V. Ustinov, Topological excitations and bound photon pairs in a superconducting quantum metamaterial, *Phys. Rev. B* **103**, 224520 (2021).

- [48] M. Trepanier, D. Zhang, L. V. Filippenko, V. P. Koshelets, and S. M. Anlage, Tunable superconducting Josephson dielectric metamaterial, *AIP Adv.* **9**, 105320 (2019).
- [49] M. Lawson, A. J. Millar, M. Pancaldi, E. Vitagliano, and F. Wilczek, Tunable Axion Plasma Haloscopes, *Phys. Rev. Lett.* **123**, 141802 (2019).
- [50] M. C. Ricci and S. M. Anlage, Single superconducting splitting resonator electrodynamics, *Appl. Phys. Lett.* **88**, 264102 (2006).
- [51] M. C. Ricci, H. Xu, R. Prozorov, A. P. Zhuravel, A. V. Ustinov, and S. M. Anlage, Tunability of superconducting metamaterials, *IEEE Trans. Appl. Supercond.* **17**, 918 (2007).
- [52] C. Kurter, A. P. Zhuravel, A. V. Ustinov, and S. M. Anlage, Microscopic examination of hot spots giving rise to nonlinearity in superconducting resonators, *Phys. Rev. B* **84**, 104515 (2011).
- [53] C. Kurter, P. Tassin, A. P. Zhuravel, L. Zhang, T. Koschny, A. V. Ustinov, C. M. Soukoulis, and S. M. Anlage, Switching nonlinearity in a superconductor-enhanced metamaterial, *Appl. Phys. Lett.* **100**, 121906 (2012).
- [54] C. Kurter, T. Lan, L. Sarytchev, and S. M. Anlage, Tunable Negative Permeability in a Three-Dimensional Superconducting Metamaterial, *Phys. Rev. Appl.* **3**, 054010 (2015).
- [55] D. Zhang, M. Trepanier, T. Antonsen, E. Ott, and S. M. Anlage, Intermodulation in nonlinear SQUID metamaterials: Experiment and theory, *Phys. Rev. B* **94**, 174507 (2016).
- [56] C. Hutter, D. Platz, E. A. Tholén, T. H. Hansson, and D. B. Haviland, Reconstructing Nonlinearities with Intermodulation Spectroscopy, *Phys. Rev. Lett.* **104**, 050801 (2010).
- [57] E. A. Tholen, D. Platz, D. Forchheimer, V. Schuler, M. O. Tholen, C. Hutter, and D. B. Haviland, Note: The intermodulation lockin analyzer, *Rev. Sci. Instrum.* **82**, 026109 (2011).
- [58] T. B. Samoilova, Nonlinear microwave effects in thin superconducting films, *Supercond. Sci. Technol.* **8**, 259 (1995).
- [59] E. A. Vopilkin, A. E. Parafin, and A. N. Reznik, Intermodulation in a microwave resonator with a high-temperature superconductor, *Tech. Phys.* **45**, 214 (2000).
- [60] D. E. Oates, S. H. Park, and G. Koren, Observation of the Nonlinear Meissner Effect in YBCO Thin Films: Evidence for a d -Wave Order Parameter in the Bulk of the Cuprate Superconductors, *Phys. Rev. Lett.* **93**, 197001 (2004).
- [61] J. C. Booth, K. Leong, S. A. Schima, J. A. Jargon, D. C. DeGroot, and R. Schwall, Phase-sensitive measurements of nonlinearity in high-temperature superconductor thin films, *IEEE Trans. Appl. Supercond.* **15**, 1000 (2005).
- [62] D. I. Mircea, H. Xu, and S. M. Anlage, Phase-sensitive harmonic measurements of microwave nonlinearities in cuprate thin films, *Phys. Rev. B* **80**, 144505 (2009).
- [63] A. P. Zhuravel, S. M. Anlage, S. K. Remillard, A. V. Lukashenko, and A. V. Ustinov, Effect of LaAlO₃ twin-domain topology on local dc and microwave properties of cuprate films, *J. Appl. Phys.* **108**, 033920 (2010).
- [64] M. T. Abuelma'atti, Harmonic and intermodulation performance of Josephson junctions, *Int. J. Infrared Millimeter Waves* **14**, 1299 (1993).
- [65] T. Dahm and D. J. Scalapino, Theory of microwave intermodulation in a high- T_c superconducting microstrip resonator, *Appl. Phys. Lett.* **69**, 4248 (1996).
- [66] T. C. L. G. Sollner, J. P. Sage, and D. E. Oates, Microwave intermodulation products and excess critical current in YBa₂Cu₃O_{7-x} Josephson junctions, *Appl. Phys. Lett.* **68**, 1003 (1996).
- [67] W. S. Hu, A. S. Thanawalla, B. J. Feenstra, F. C. Wellstood, and S. M. Anlage, Imaging of microwave intermodulation fields in a superconducting microstrip resonator, *Appl. Phys. Lett.* **75**, 2824 (1999).
- [68] A. P. Zhuravel, A. V. Ustinov, D. Abraimov, and S. M. Anlage, Imaging local sources of intermodulation in superconducting microwave devices, *IEEE Trans. Appl. Supercond.* **13**, 340 (2003).
- [69] B. Abdo, O. Suchoi, E. Segev, O. Shtempluck, M. Blencowe, and E. Buks, Intermodulation and parametric amplification in a superconducting stripline resonator integrated with a dc-SQUID, *Europhys. Lett.* **85**, 68001 (2009).
- [70] E. K. Pease, B. J. Dober, and S. K. Remillard, Synchronous measurement of even and odd order intermodulation distortion at the resonant frequency of a superconducting resonator, *Rev. Sci. Instrum.* **81**, 024701 (2010).
- [71] J. Aumentado, Superconducting parametric amplifiers: The state of the art in Josephson parametric amplifiers, *IEEE Microw. Mag.* **21**, 45 (2020).
- [72] A. Roy and M. Devoret, Introduction to parametric amplification of quantum signals with Josephson circuits, *C. R. Phys.* **17**, 740 (2016).
- [73] A. Wolf, J. B. Swift, H. L. Swinney, and J. A. Vastano, Determining Lyapunov exponents from a time series, *Physica D* **16**, 285 (1985).
- [74] D. Zhang, Radio frequency superconducting quantum interference device meta-atoms and metamaterials: Experiment, theory, and analysis, Ph.D. thesis, University of Maryland, 2016, <https://drum.lib.umd.edu/handle/1903/18805>.